



Heat treatment effects in oxygen-doped β -Li₃PS₄ solid electrolyte prepared by wet chemistry method

Jiuyong Li^{1,2,3} · Weiming Liu^{1,2} · Xiaofeng Zhang^{1,2} · Yibo Ma^{1,2} · Youxiu Wei^{1,2} · Ziyi Fu^{1,2} · Jiaming Li^{1,2} · Yue Yan^{1,2}

Received: 18 October 2020 / Revised: 9 January 2021 / Accepted: 11 January 2021 / Published online: 21 January 2021
© The Author(s), under exclusive licence to Springer-Verlag GmbH, DE part of Springer Nature 2021

Abstract

For advanced all-solid-state lithium batteries, the solid electrolyte is one of the most critical components that significantly affect battery performance. Herein, solid electrolytes $75\text{Li}_2\text{S} \cdot (25-x)\text{P}_2\text{S}_5 \cdot x\text{P}_2\text{O}_5$ (mol%) are successfully prepared via wet chemistry method. Their XRD patterns show that only the crystalline phase β -Li₃PS₄ is detected for $x = 0, 1, 2, 3, 5$ mol% and the highest room-temperature ionic conductivity of $2.53 \times 10^{-4} \text{ S cm}^{-1}$ is obtained when $x = 2$. Next, effects of heat treatment on the structure and electrochemical performance of $75\text{Li}_2\text{S} \cdot 23\text{P}_2\text{S}_5 \cdot 2\text{P}_2\text{O}_5$ are systematically studied. The thermal stability, morphology, structure, and crystal phase of the $75\text{Li}_2\text{S} \cdot 23\text{P}_2\text{S}_5 \cdot 2\text{P}_2\text{O}_5$ electrolyte heated at different temperatures are characterized by thermogravimetric analysis and differential scanning calorimetry (TGA-DSC), SEM, N₂ adsorption/desorption, Raman, and XRD. The $75\text{Li}_2\text{S} \cdot 23\text{P}_2\text{S}_5 \cdot 2\text{P}_2\text{O}_5$ electrolyte heat-treated at 320 °C exhibits the highest ionic conductivity of $2.72 \times 10^{-4} \text{ S cm}^{-1}$, the lowest electronic conductivity of $4.8 \times 10^{-9} \text{ S cm}^{-1}$, and excellent electrochemical stability against the metallic lithium electrode. When the heat treatment temperature further increases from 320 to 500 °C, the electrolyte partially decomposes into Li₄P₂S₆ and Li₂S. Our results underscore the importance of heat treatment for the synthesis and performance optimization of solid electrolytes for the application of high-energy solid-state batteries.

Keywords Solid electrolyte · β -Li₃PS₄ · Oxygen doping · Heat treatment · Wet chemistry method

Introduction

Lithium-ion batteries are important for a wide variety of applications ranging from consumer electronics, automotive propulsion to stationary load leveling for intermittent power generation, such as wind and solar energy [1, 2]. However, conventional lithium-ion batteries with organic liquid electrolyte still have the drawbacks, i.e., safety concerns, leakage and corrosion, and technological limitations for miniaturization [3]. All-solid-state batteries with a sulfide-based solid-state electrolyte are believed to be one of the best solutions because of the high ionic conductivity and unique mechanical properties of the

sulfide-based solid electrolytes [4, 5]. In the last few years, the research interest from both scholar and industrial sectors in Li₂S-P₂S₅ binary system electrolytes has grown steadily [6].

For the Li₂S-P₂S₅ system, different ratios of Li₂S and P₂S₅ starting materials can generate the final products with different proportions of PS₄³⁻ and P₂S₇⁴⁻ structural units, which determines the electrochemical properties of the electrolyte material [7]. In the binary system, $75\text{Li}_2\text{S} \cdot 25\text{P}_2\text{S}_5$ (mol%) (Li₃PS₄) crystalline phase is the most chemically stable and likely to be one of the most suitable electrolyte materials for use in all-solid-state batteries with metal lithium negative electrode [8–10]. Li₃PS₄ has three kinds of crystal structures in the phase diagram, including α , β , and γ phases. The stable γ phase with a low ionic conductivity of $3 \times 10^{-7} \text{ S cm}^{-1}$ at room temperature would transform to the metastable β phase with the fast lithium-ion transport path when heated to 195 °C, and then transformed to the even higher temperature α phase at 473 °C. Reversely, as the temperature cools down to room temperature, α phase would revert back to the γ phase directly [11]. For bulk Li₃PS₄, the desired β phase with high ionic conductivity cannot exist steadily at room temperature [11]. However, as the Li₃PS₄ size decreases

✉ Yue Yan
yue.yan@biam.ac.cn

¹ Beijing Institute of Aeronautical Materials, Beijing 100095, China
² Beijing Engineering Research Center of Advanced Structural Transparency for the Modern Traffic System, Beijing 100095, China
³ School of Materials Science and Engineering, Henan University of Science and Technology, Luoyang 471000, Henan, China

to nanoscale, its crystalline property changes significantly [9]. Liu et al. [9] first reported the preparation of a room-temperature stable nanoporous β - Li_3PS_4 solid electrolyte by liquid phase synthesis, and its ionic conductivity reaches $1.6 \times 10^{-4} \text{ S}\cdot\text{cm}^{-1}$, which is three orders of magnitude higher than bulk γ - Li_3PS_4 . With the similar process, various sulfide solid electrolytes such as β - Li_3PS_4 , $\text{Li}_7\text{P}_3\text{S}_{11}$, and $\text{Li}_7\text{P}_2\text{S}_8\text{I}$ have been synthesized via wet chemical method.

As a mild and economical preparation method for the Li_2S - P_2S_5 solid electrolyte, wet chemical method has attracted much attention in recent years [12]. It can effectively prepare nanoparticles with controllable particle size and morphology by utilizing the diversity and controllability of the solution. In a typical wet chemical synthesis, the starting materials (e.g., Li_2S and P_2S_5) are dispersed in organic solvents, such as tetrahydrofuran (THF) [9, 13], acetonitrile (ACN) [14], 1,2-dimethoxyethane (DME) [15], ethyl acetate (EA) [16], and ethyl propionate (EP) [17], and can react with each other to obtain the desired solid electrolyte. In the wet chemical method, with the solvent removal and subsequent crystallization process, heat treatment plays a vital role in the synthesis of Li_2S - P_2S_5 solid electrolyte and the improvement of its performance. Yubuchi et al. [18] revealed the effects of heat treatment on the crystallinities and ionic conductivities in the synthesis process of argyrodite sulfide-based solid electrolytes with THF and ethanol and showed that the ratio of the amorphous and crystal phases strongly affects the conductivity of the argyrodite electrolyte. Nevertheless, to the best of our knowledge, there is almost no systematic and comprehensive studies on the influences of heat treatment on the morphology, structural composition, and electrochemical performance of sulfur-based solid electrolytes (especially Li_3PS_4), as well as their interrelationships, which is very important to deepen the understanding of heat treatment effects in electrolyte properties.

Most of the solvents used in the synthesis of the Li_2S - P_2S_5 system electrolyte are oxygen-containing polar organic liquids, and it is unavoidable to bring oxygen into the solid electrolytes [19]; that is, it is impossible to obtain absolutely pure oxygen-free electrolytes. Based on this, we used P_2O_5 as the oxygen source to study the influence of different oxygen doping levels on the ionic conductivity of $75\text{Li}_2\text{S}\cdot(25-x)\text{P}_2\text{S}_5\cdot x\text{P}_2\text{O}_5$ ($x = 0, 1, 2, 3, 5$ mol%) electrolytes, and the effects of heat treatment on the structure and electrochemical properties of $75\text{Li}_2\text{S}\cdot 23\text{P}_2\text{S}_5\cdot 2\text{P}_2\text{O}_5$ with optimized oxygen doping were investigated and discussed based on the thermal stability, morphology, and crystal phases.

Experiment

Material synthesis and characterization

In a typical synthesis, stoichiometric amounts of Li_2S (99.9%, Alfa Aesar), P_2S_5 ($\geq 99\%$, Sinopharm Chemical) and P_2O_5

(99.99%, Macklin) as raw materials were mixed in anhydrous tetrahydrofuran (THF, 99.5%, extra dry with molecular sieves, H_2O content of ≤ 50 ppm, Energy Chemical) in an argon-filled glove box (O_2 and H_2O content of < 0.1 ppm). The mixtures were then stirred for 24 h at room temperature. The white precipitation was separated by centrifuge with 5000 rpm for 5 min and washed with THF three times. As-synthesized precipitation was dried under vacuum at room temperature for the removal of excess THF. The obtained white powder is denoted as LPSO-THF. Then, the LPSO-THF sample was sequentially dried at 80, 90, 100, 120, and 140 °C for 10 min under vacuum to remove the residual THF. The crystalline electrolyte $75\text{Li}_2\text{S}\cdot(25-x)\text{P}_2\text{S}_5\cdot x\text{P}_2\text{O}_5$ ($x = 0, 1, 2, 3, 5$ mol%) was obtained by heating the dried sample at 140 °C for 1 h. Heat treatments of the dried sample with optimal oxygen doping amount were conducted in a quartz tube furnace filled with argon gas at different temperatures of 140, 200, 260, 320, 380, 440, and 500 °C (labeled as LPSO-140, LPSO-200, LPSO-260, LPSO-320, LPSO-380, LPSO-440, LPSO-500 samples), respectively, for 1 h.

Thermogravimetric analysis (TGA) and differential scanning calorimetry (DSC) were performed using a synchronous thermal analyzer (TGA-DSC, STA 499 F3, NETZSCH) under a stream of dry nitrogen with a heating rate of $5 \text{ }^\circ\text{C min}^{-1}$. Nitrogen adsorption and desorption isotherms were measured at $-196 \text{ }^\circ\text{C}$, using a TRISTAR II 3020M analyzer utilizing Barrett-Emmett-Teller (BET) calculations for surface area from the desorption branch of the isotherm. SEM images were conducted on a cold field emission scanning electron microscope (SEM, Hitachi SU-8010). Structures of the prepared powders were characterized using X-ray diffraction (XRD, D8 Advance, Bruker) with copper $\text{K}\alpha$ radiation ($\lambda = 1.54178 \text{ \AA}$). Diffraction data were collected in 0.02° steps from 7° to 50° in 2θ . The structural units of samples were identified by using a microlaser Raman spectrometer (Raman, JY HR-800, Horiba) with a 514-nm laser. All characterizations were handled with special care to avoid contact with air and moisture.

Electrochemical testing

The ionic conductivity of the pelletized samples was measured by electrochemical impedance spectroscopy (EIS). The solid electrolyte powders (0.1 g) were pressed under 499 MPa in a polycarbonate-made tube with a 10-mm diameter at room temperature. Stainless steel (SUS) rods were used as blocking electrodes on both sides of the pellets. EIS was carried out using an electrochemical workstation (660E, CHI) in the frequency from 1 Hz to 1 MHz at the amplitude of 5 mV over a temperature range of -55 to $80 \text{ }^\circ\text{C}$ and the sample was held at each temperature for 1 h prior to the impedance measurement. The typical SUS/solid electrolyte (SE)/SUS cells were also served for the electronic conductivity measurements to

determine the dominant mobile ions in the sample compared with the ionic conductivity, and the cells were applied a constant DC voltage 1 V and the current was recorded.

The interfacial stability of metal lithium electrode with typical electrolyte pellets was investigated by monitoring the voltage evolution in symmetrical Li/SE/Li cells by a battery test system (CT2001A, LAND) with a current density of 0.1 mA cm^{-2} at room temperature. The symmetrical Li/SE/Li cells were assembled by cold-pressing process as same as EIS test. These cells were then transferred to our home-made mold at a lower pressure by thread and put into an argon-filled thermotank in order to avoid the effects of ambient temperature changes. The electrochemical stability of the pelletized electrolytes was evaluated by cyclic voltammetry (CV). A 300-nm-thick gold film deposited on aluminum foil by magnetron sputtering as the working electrode was attached to one side of the pellet. A lithium foil serving as the counter/reference electrode was also attached to the other side of the pellet. The potential sweep was performed with a scanning

rate of 1 mV s^{-1} between -0.5 and 5 V at room temperature. All testing processes were conducted at an argon atmosphere.

Results and discussion

Oxygen doping

Figure 1a displays the XRD patterns of the $75\text{Li}_2\text{S}\cdot 25\text{P}_2\text{S}_5$ sample dried at different temperatures and $75\text{Li}_2\text{S}\cdot(25-x)\text{P}_2\text{S}_5\cdot x\text{P}_2\text{O}_5$ ($x=0, 1, 2, 3, 5 \text{ mol}\%$) samples heat-treated at 140°C for 1 h. No obvious peaks are detected for dried $75\text{Li}_2\text{S}\cdot 25\text{P}_2\text{S}_5$ sample, indicating its amorphous state. Similarly, all dried $75\text{Li}_2\text{S}\cdot(25-x)\text{P}_2\text{S}_5\cdot x\text{P}_2\text{O}_5$ ($x=1, 2, 3, 5 \text{ mol}\%$) samples also show amorphous features (not shown). Then, the obtained amorphous powders were heat-treated at 140°C for 1 h. As shown in Fig. 1a, their several crystalline peaks indicate the formation of crystalline phase. The XRD patterns of all heat-treated samples can be well indexed to the

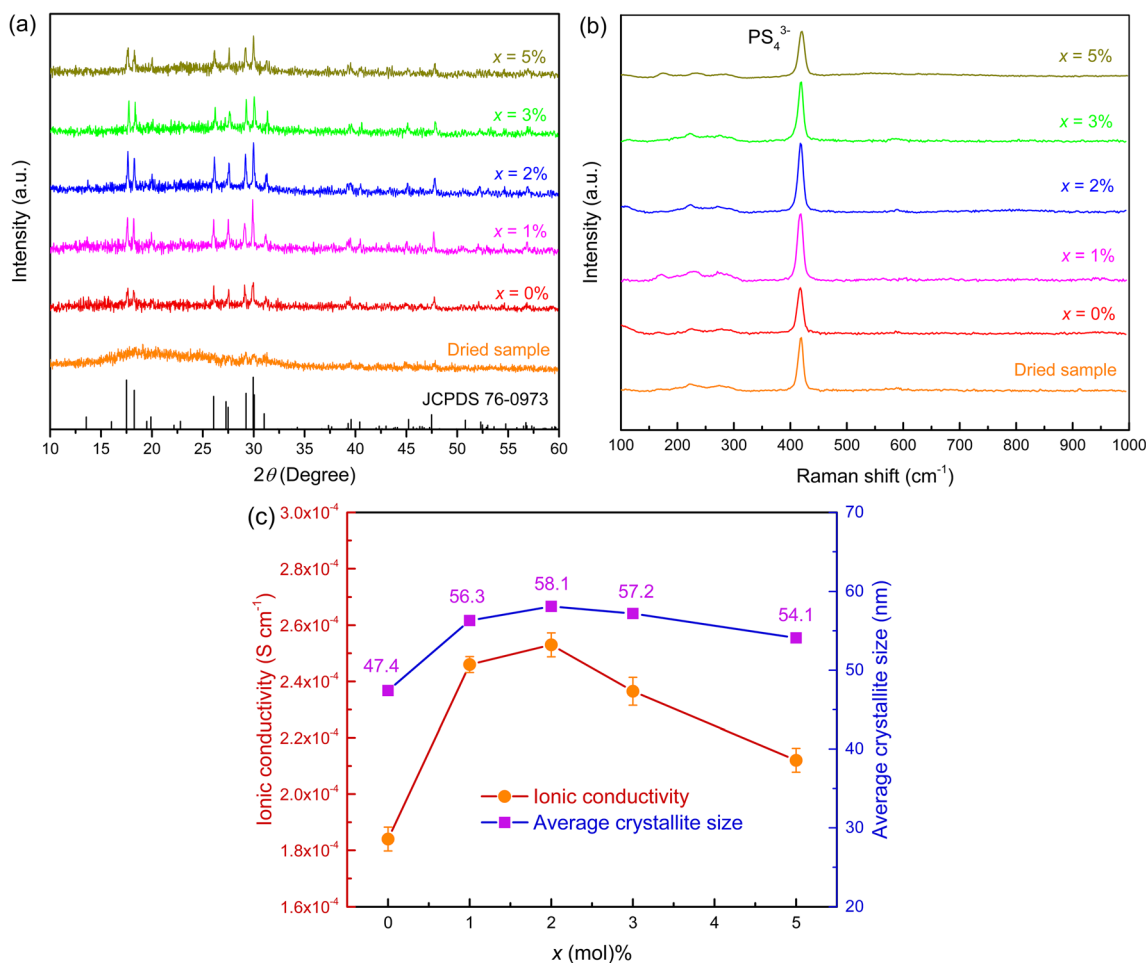


Fig. 1 a XRD patterns and b the corresponding Raman spectra of the dried $75\text{Li}_2\text{S}\cdot 25\text{P}_2\text{S}_5$ sample and heat-treated $75\text{Li}_2\text{S}\cdot(25-x)\text{P}_2\text{S}_5\cdot x\text{P}_2\text{O}_5$ ($x=0, 1, 2, 3, 5 \text{ mol}\%$) samples. c The variation of room-temperature

ionic conductivities and the average crystallite size with the value of x in $75\text{Li}_2\text{S}\cdot(25-x)\text{P}_2\text{S}_5\cdot x\text{P}_2\text{O}_5$

crystalline phase β -Li₃PS₄ (JCPDS 76-0973) and no other phases are detected. In addition, it is worth noting that compared with the sample with $x = 0$, the XRD peak intensity of the doped P₂O₅ samples is obviously increased, implying that the crystallinity of the sample may be changed. Therefore, we fitted the XRD patterns and calculated the average crystallite sizes of the 75Li₂S·(25- x)P₂S₅· x P₂O₅ electrolyte samples according to the Scherrer equation, as shown in Fig. 1c. As the doping amount of P₂O₅ increases from $x = 0$ to 2, the average crystallite size of the β -Li₃PS₄ crystal increases significantly, and then decreases slightly with further increase to $x = 5$. This implies that under the same conditions, the incorporation of a small amount of P₂O₅ enhances the crystallinity of β -Li₃PS₄, while even higher doping amounts could be detrimental to its crystallinity, consistently with the results obtained by mechanical milling [20].

The Raman spectra were employed to further elucidate the structure variations of a series of electrolytes, as demonstrated in the Fig. 1b. It can be seen that in the 150–300 cm⁻¹ region, there are three peaks at 176, 221, and 284 cm⁻¹ for $x = 0, 1, 5$ mol% that are deformation modes of S-P-S in PS₄³⁻ units [21–24]. Moreover, we noticed that the Raman spectra of samples of $x = 2, 3$ mol% and dried samples do not show the peak at 176 cm⁻¹. The reason is not yet clear. However, the appearance of the peak at 176 cm⁻¹ in this study seems to be random and not affected by the P₂O₅ doping content. More importantly, the characteristic peak of the PS₄³⁻ units' symmetric stretching at around 418 cm⁻¹ is observed in electrolyte samples for all compositions ($x = 0, 1, 2, 3, 5$ mol%) [9, 21, 25]. This results suggest that a small amount of P₂O₅ ($x \leq 5$ mol%) doped into the 75Li₂S·25P₂S₅ system does not change the existence of PS₄³⁻ units and no other groups are detected in the wide range of 100–1000 cm⁻¹ under the limitation of the Raman spectra, which agree with previous reports [20, 25].

In order to evaluate the effect of P₂O₅ doping on ionic transport behavior, we measured the ionic conductivities of obtained 75Li₂S·(25- x)P₂S₅· x P₂O₅ crystalline samples at room temperature. The dependence of lithium-ion conductivities on the value of x in 75Li₂S·(25- x)P₂S₅· x P₂O₅ is shown in Fig. 1c. As the doping amount of P₂O₅ increases, the ionic conductivity of 75Li₂S·(25- x)P₂S₅· x P₂O₅ electrolyte increases rapidly to the maximum peak value of 2.53×10^{-4} S cm⁻¹ at $x = 2$, and then decreases with further increasing x to 5. As is well known, β -Li₃PS₄ phase is a good lithium ionic conductor, and its large interstitials constructed by the zig-zag arrangements of the PS₄ tetrahedra facilitate the movement of lithium ions [11]; thus, β -Li₃PS₄ phase with high crystallinity is beneficial to the enhancement of ionic conductivity [9, 26]. Consequently, when x increases from 0 to 2, the ionic conductivity of the sample increases significantly. Moreover, it was also reported that the doped oxygen in β -Li₃PS₄ acts as a connector of 2D paths, driving the transport of ions from two-dimensional to three-

dimensional, which can significantly improve the ionic conductivity [27]. When the P₂O₅ doping amount is further increased to 5 mol%, the crystallinity of the sample only slightly attenuates, yet the ionic conductivity is obviously reduced. In addition to the effect of crystallinity, an even larger substitution amount could form oxysulfide units and PO₄ units with non-bridging oxygen, which work as strong traps for lithium-ion conduction [28]. Therefore, the highest conductivity is obtained at a low doping amount of $x = 2$.

As reported, an appropriate amount of oxygen doping can simultaneously improve the ion transport properties and room-temperature structural stability of the crystalline β -Li₃PS₄ solid electrolyte [27, 29, 30]. For the ion transport properties, the combination of the bond-valence method and the density functional theory calculation reveals that oxygen doping at sulfur site significantly improves the kinetic properties [29]. It is easier for lithium to jump around oxygen atom because there is a larger space around oxygen than around sulfur. The radial distribution function results of Klerk et al. [30] also show that oxygen doping changes the distribution of lithium ions in the crystal, which is beneficial to the diffusion of lithium ions in β -Li₃PS₄. For the room-temperature structural stability, Wang et al. [27] calculated the total energies of β -Li₃PS₄ and γ -Li₃PS₄ structures with different oxygen doping concentrations in order to compare the phase stability of β and γ phases. Their results showed that as the oxygen doping concentration increases, the β and γ phases gradually exhibit close energies, and the β phase energy of Li₃PS_{3.75}O_{0.25} is even lower than that of the γ phase by 0.002 eV per formula unit; in other words, the β phase doped with 2.5 mol% oxygen can theoretically be stabilized at room temperature. This doping amount is quite close to the optimal doping amount of 2 mol% in this study. In addition, from the XRD patterns in Fig. 1a, it can be seen that all doped crystalline samples contained room-temperature stable β phase, which may be due to the combined effect of oxygen doping and the nanoporous structure brought about by wet chemical method [9].

Heat treatment

Structure and morphology

As discussed above, $x = 2$ was selected as the optimal doping amount. Based on this, the effects of heat treatment on the structure and electrochemical properties of 75Li₂S·23P₂S₅·2P₂O₅ are systematically studied. Figure 2 shows the TGA-DSC curves of the LPSO-THF sample dried under vacuum at room temperature. As shown, the DSC curve displays two distinct endothermic peaks at around 90 °C and 140 °C observed on overall heating process from room temperature to 550 °C, which associated with the weight loss due to the removal of THF. The corresponding TGA curve shows that the two losses of the sample weight account for 35.54% and

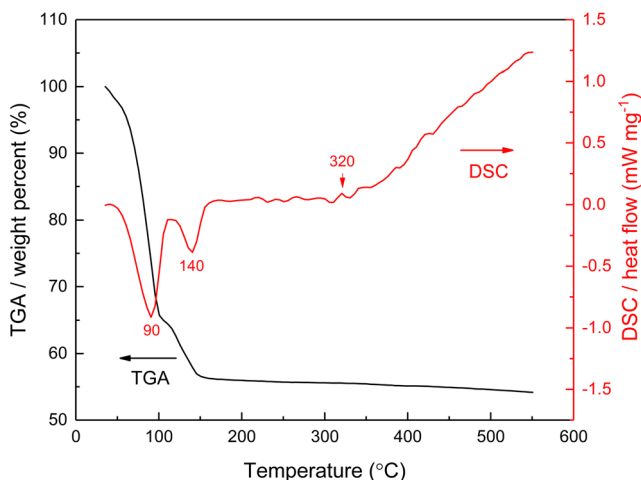


Fig. 2 TGA-DSC curves of the LPSO-THF sample at $5\text{ }^{\circ}\text{C min}^{-1}$ under N_2

8.33% of its initial weight, respectively. After the temperature increases over $320\text{ }^{\circ}\text{C}$, a sustained release of heat is observed from the DSC curve, and in the corresponding TGA curve, the weight decreases slowly. This indicates that the sample undergoes an exothermic decomposition process when the heat treatment temperature exceeds $320\text{ }^{\circ}\text{C}$.

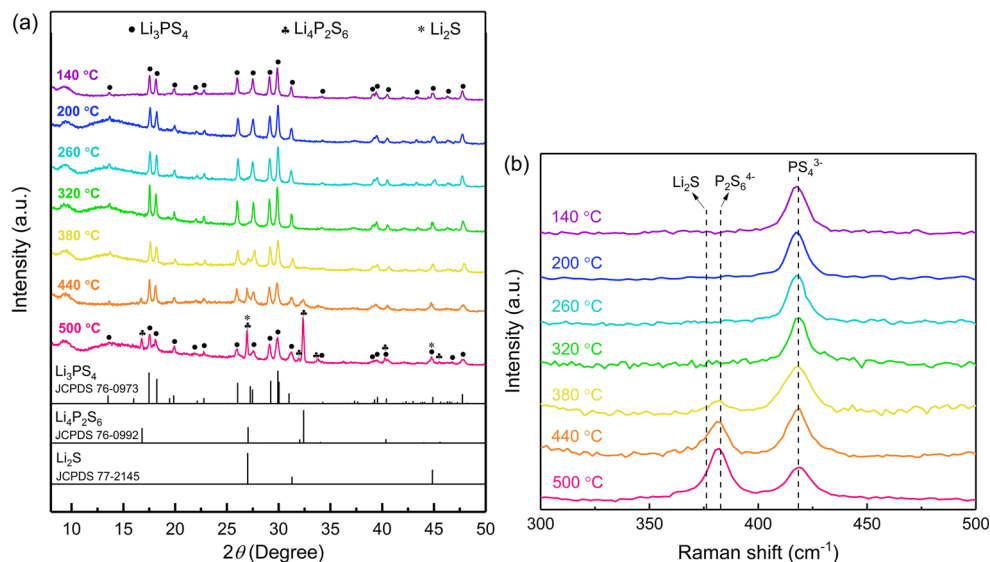
The XRD patterns and Raman spectra of the powder samples obtained at different heat treatment temperatures are recorded and depicted in Fig. 3. As shown in Fig. 3a, indexed XRD patterns of the Li_3PS_4 (JCPDS 76-0973), $\text{Li}_4\text{P}_2\text{S}_6$ (JCPDS 76-0992), and Li_2S (JCPDS 77-2145) phases are attached for comparison. The patterns can be well indexed to the single $\beta\text{-Li}_3\text{PS}_4$ phase in the samples heat-treated at 140, 200, 260, and $320\text{ }^{\circ}\text{C}$. As the heat treatment temperature increases from 140 to $320\text{ }^{\circ}\text{C}$, the crystallization peak strength increases gradually. With a further increase of the temperature, $\text{Li}_4\text{P}_2\text{S}_6$ and Li_2S phases are simultaneously observed. As reported,

both the $\text{Li}_4\text{P}_2\text{S}_6$ and Li_2S phase exhibit extremely low lithium-ion conductivity at room temperature, and they are not conducive to improve the ionic conductivity of the electrolytes [31, 32]. In addition, it is noteworthy that when the heat treatment temperature reaches $500\text{ }^{\circ}\text{C}$, the obtained Li_3PS_4 is still β phase, rather than the low Li-conductive γ phase as reported by Chen et al. [33] for heat treatment above $400\text{ }^{\circ}\text{C}$. This could be attributed to the role of oxygen doping to stabilize the β phase structure [27].

The structure variations of the electrolytes were further illustrated by the Raman spectra, as demonstrated in the Fig. 3b. All samples show a peak at around 418 cm^{-1} , which belongs to symmetric stretching of the P-S bonds in the PS_4^{3-} units [21]. The samples heated at 380, 440, and $500\text{ }^{\circ}\text{C}$ show additional peaks at around 376 and 382 cm^{-1} , which could be attributed to the motion of the Li sublattice in the Li_2S unit and symmetric stretching of the P-S bonds in the $\text{P}_2\text{S}_6^{4-}$ units of $\text{Li}_4\text{P}_2\text{S}_6$, respectively [10, 21]. Moreover, as the heat treatment temperature increases, the intensity of the Li_2S and $\text{P}_2\text{S}_6^{4-}$ peaks increases gradually, while that of the PS_4^{3-} peak decreases. This is consistent with the XRD results in Fig. 3a.

Figure 4 displays the morphologies of as-prepared powder samples treated at different temperatures. Figure 4a to h correspond to the sample LPSO-THF to LPSO-500, respectively. It can be seen from Fig. 4a that the sample LPSO-THF is mainly composed of irregular block-like particles, and the surface of the particles is smooth and non-porous because abundant THF molecules remain in the sample. After vacuum drying and heat treatment at $140\text{ }^{\circ}\text{C}$, the THF molecules are removed, and the electrolyte particles aggregate and integrate to form block-like particles with an average size of about $10\text{ }\mu\text{m}$, as shown in Fig. 4b. Furthermore, a large number of slit-shaped pores are observed on the surface of these particles from the inserted image, which is attributed to the removal of

Fig. 3 a XRD patterns and b the corresponding Raman spectra of the powder samples obtained at different heat treatment temperatures



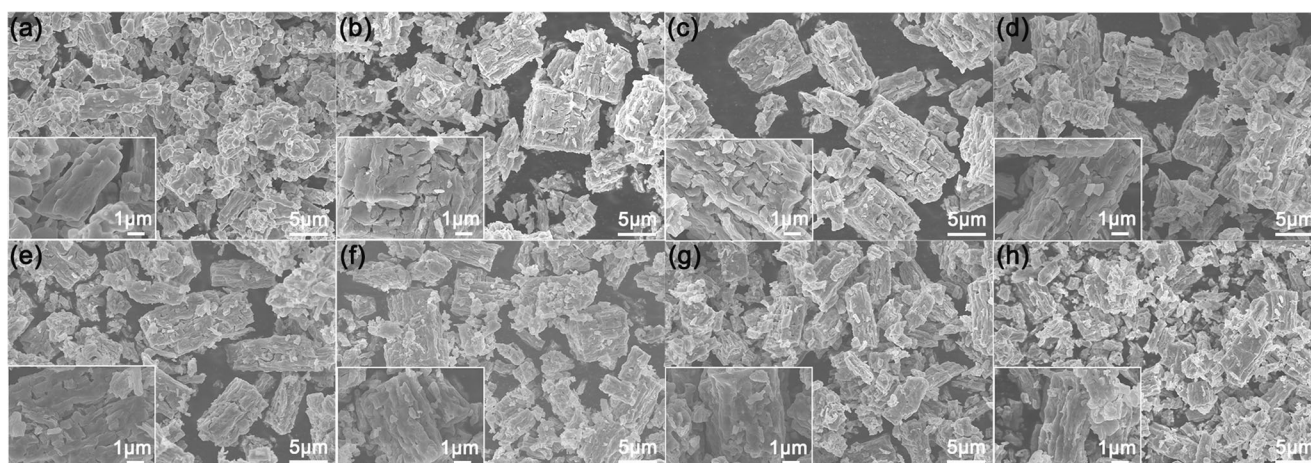


Fig. 4 SEM images of samples **a** LPSO-THF, **b** LPSO-140, **c** LPSO-200, **d** LPSO-260, **e** LPSO-320, **f** LPSO-380, **g** LPSO-440, and **h** LPSO-500. The inserted image in the lower left corner is a high-magnification of the surface of the electrolyte particles

solvent molecules and the aggregation of nanocrystals. With the temperature increasing from 140 to 320 °C, the morphology of the electrolyte particles is little changed, but the density of slit-shaped pores on the particle surface slightly diminishes. When temperature further increases to 500 °C, the particle size significantly reduces, and the surface slits almost disappear, which is related to the particle breakage caused by slit or crack propagation at elevated temperature.

We conducted nitrogen adsorption and desorption measurements to further examine the porous properties of the sulfide electrolyte samples heat-treated at different temperature. As shown in Fig. 5a, nitrogen adsorption/desorption isotherms of all samples are identified as a type III isotherm with a type H3 hysteresis loop [34], which does not exhibit any limiting adsorption at high relative pressures. And this is consistent with the characteristic of mesoporous materials. Obviously, nitrogen volume adsorbed rapidly drops with the heat treatment temperature increasing. Moreover, The BET surface area of these samples was calculated from nitrogen isotherms at

– 196 °C, and the heat treatment temperature dependence of the BET surface area is exhibited in Fig. 5b. At 140 °C, the BET surface area of the sample is 28.734 m² g⁻¹, which is much higher than that of β-Li₃PS₄ obtained at the same heating temperature in the reference [9]. This could be attributed to the process of drying step by step under vacuum to further remove the solvent. As the heat treatment temperature increases from 140 to 500 °C, the BET surface area of the sample gradually decreases and eventually remains at a lower stable level. This is consistent with the variation of the pores on the surface of particles observed from the SEM in Fig. 4.

Electrochemical properties

The ionic conductivities of the electrolyte samples heat-treated at various temperatures were evaluated by EIS measurement. Figure 6a displays the Nyquist plots of the electrolyte pellets at room temperature. The Nyquist plots of the LPSO-380, LPSO-440, and LPSO-500 samples consist of an

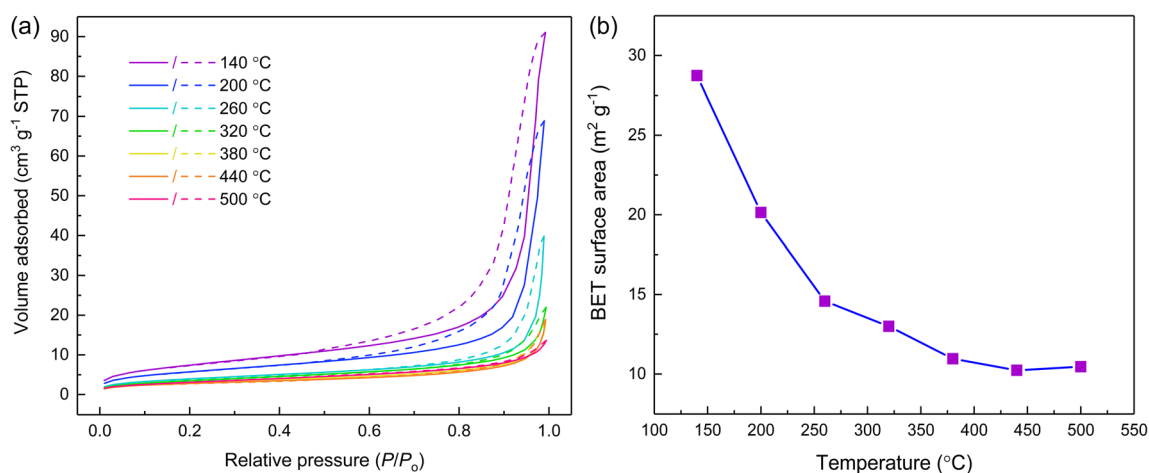


Fig. 5 **a** Nitrogen adsorption (solid lines) and desorption (dashed lines) isotherms and **b** heat treatment temperature dependence of BET surface area of the obtained powder samples

arc at high frequency due to the interface transfer resistances and a capacitive tail at low frequency due to the ionic diffusion at the electrode interface [35]. The total resistance (bulk and interface transfer resistances) is used to calculate the ionic conductivity. In addition, the Nyquist plots of the LPSO-140, LPSO-200, LPSO-260, and LPSO-320 samples do not exhibit the full arc at high frequency due to the lower resistance. The resistance is estimated by the value of Z' at the intercept with the real axis obtained by linear fitting.

Figure 6b shows the ionic conductivity of electrolytes at room temperature as a function of heat treatment temperatures. As the heat treatment temperature increases from 140 to 320 °C, the ionic conductivity of the electrolyte first decreases slightly and then increases, reaching a maximum of $2.72 \times 10^{-4} \text{ S cm}^{-1}$ at 320 °C. The variation trend is unexpected, and it may be attributed to two factors BET surface area and crystallinity of the sample. The surface conductivity of nanoporous $\beta\text{-Li}_3\text{PS}_4$ declines with the decrease of BET surface area [9] and the increase of electrolyte crystallinity is conducive to improve the ionic conductivity in the bulk lattice of $\beta\text{-Li}_3\text{PS}_4$ phase [26]. Their combined effect may be ultimately responsible for the variation of ionic conductivity between 140 and 320 °C. As the heat treatment temperature exceeds 320 °C, the ionic conductivity of the sample drops rapidly. This is assigned to the decomposition of $\beta\text{-Li}_3\text{PS}_4$ crystal and the formation of poor lithium ionic conductivity materials $\text{Li}_4\text{P}_2\text{S}_6$ and Li_2S .

It has been reported that high electronic conductivity promotes the formation and growth of lithium dendrites in $\text{Li}_7\text{La}_3\text{Zr}_2\text{O}_{12}$ and amorphous Li_3PS_4 solid electrolytes; therefore, lowering the electronic conductivity of solid electrolytes is critical for the success of all-solid-state lithium batteries [36]. To evaluate the electronic blocking property, we measured the electronic conductivities of

electrolyte samples heat-treated at various temperatures by a DC polarization measurement at room temperature. Figure 7a shows the current-time curves of the SUS/SE/SUS symmetric cells with an applied voltage of 1 V. All cells exhibit the similar behaviors. The current quickly decreases in the initial stage due to the polarization process and then reaches a steady state. At this steady state, the current is originated only from the contribution of the electrons. The electronic conductivity of electrolytes determined by this approach as a function of heat treatment temperatures is shown in Fig. 7b. Interestingly, the variation trend of the electronic conductivity is opposite to that of the ionic conductivity of electrolytes in Fig. 6b. Analogous phenomenon was also found in report of Yu et al. [37] who investigated the effect of doping amount of the $\text{LiO}_2\text{-SiO}_2\text{-B}_2\text{O}_3$ glass on ionic and electronic conductivity of solid electrolyte $\text{Li}_{0.5}\text{La}_{0.5}\text{TiO}_3$ prepared by solid-state reaction method. However, there is still no reasonable explanation for this phenomenon, and further research is needed. The electronic conductivities of the representative LPSO-140, LPSO-320, and LPSO-500 samples are 7×10^{-9} , 4.8×10^{-9} , and $6.4 \times 10^{-8} \text{ S cm}^{-1}$, respectively, which are much lower than their ionic conductivities measured by AC impedance method, indicating that the prepared samples are good ionic conductors [16]. More importantly, among all the samples, the LPSO-320 sample has the lowest electronic conductivity, which may be favorable to suppress the formation and growth of lithium dendrites in the solid electrolytes in the DC polarization [36].

Figure 8a shows the Arrhenius conductivity plots of the representative LPSO-140, LPSO-320, and LPSO-500 samples measured in the temperature range from -55 to 80 °C. The activation energies of samples for lithium-ion conduction

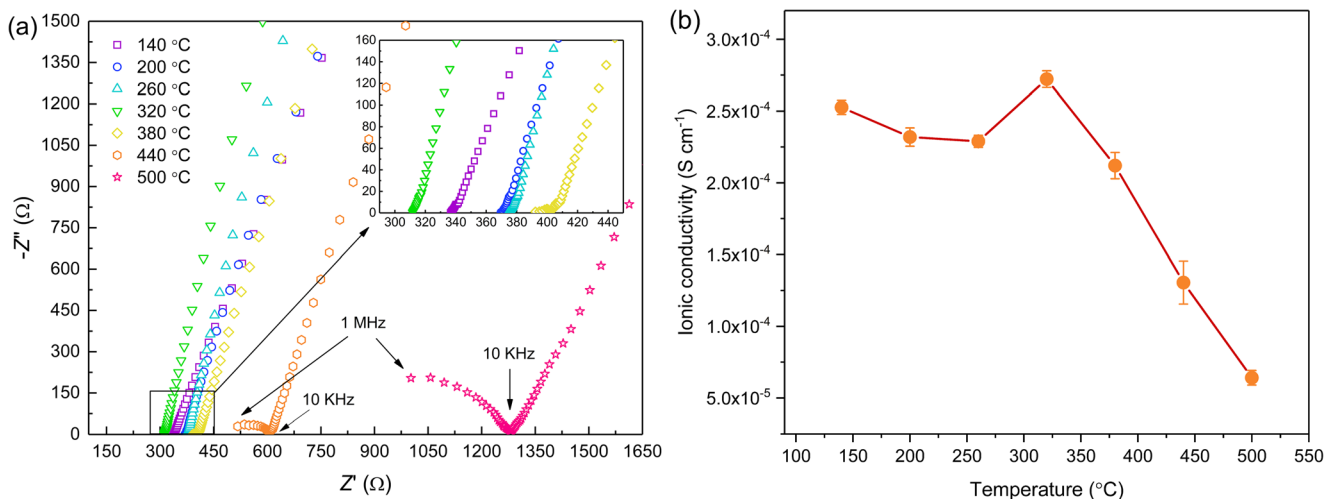


Fig. 6 a Nyquist plots of the electrolytes treated by heating at various temperatures and the inset is amplified image of the rectangular area and b the room-temperature ionic conductivity of electrolytes as a function of heat treatment temperatures

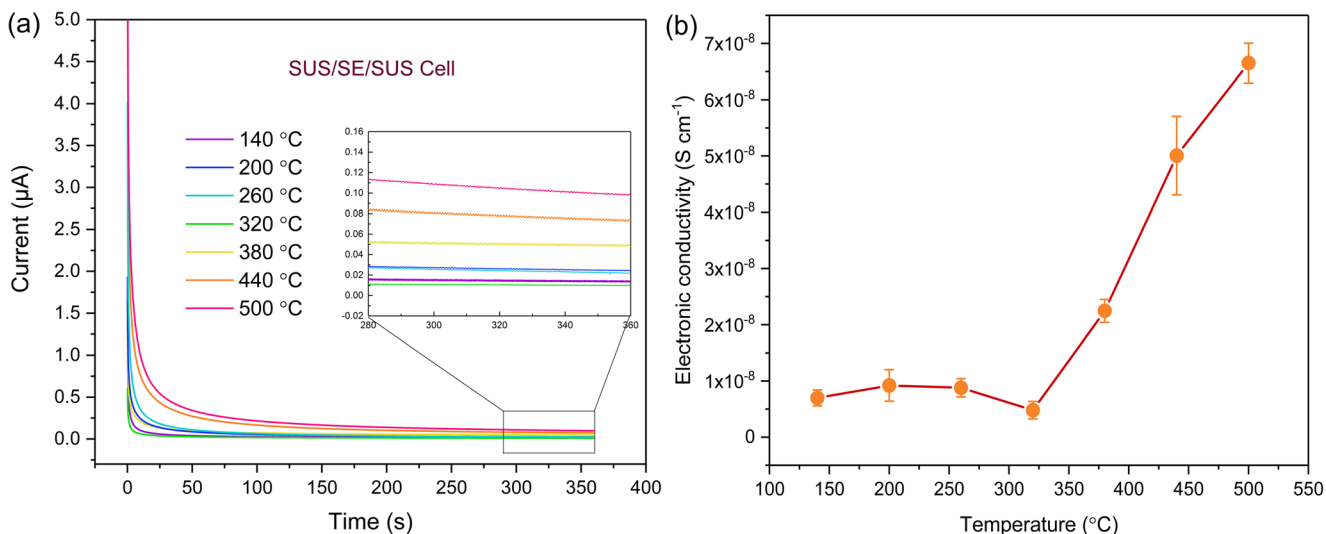


Fig. 7 **a** Current-time curves of SUS/SE/SUS symmetric cells applying a DC constant voltage of 1 V and the inset is amplified image of the rectangular area and **b** the room-temperature electronic conductivity of electrolytes as a function of heat treatment temperatures

were calculated from the slopes of the linear plots using the following Arrhenius equation:

$$\sigma = A \exp(-E_a/kT) \quad (1)$$

where E_a is the activation energy, A is the pre-exponential factor, k is the Boltzmann constant, and T is the absolute temperature. The calculated activation energies of the LPSO-140, LPSO-320, and LPSO-500 sample are 29.89, 32.37, and

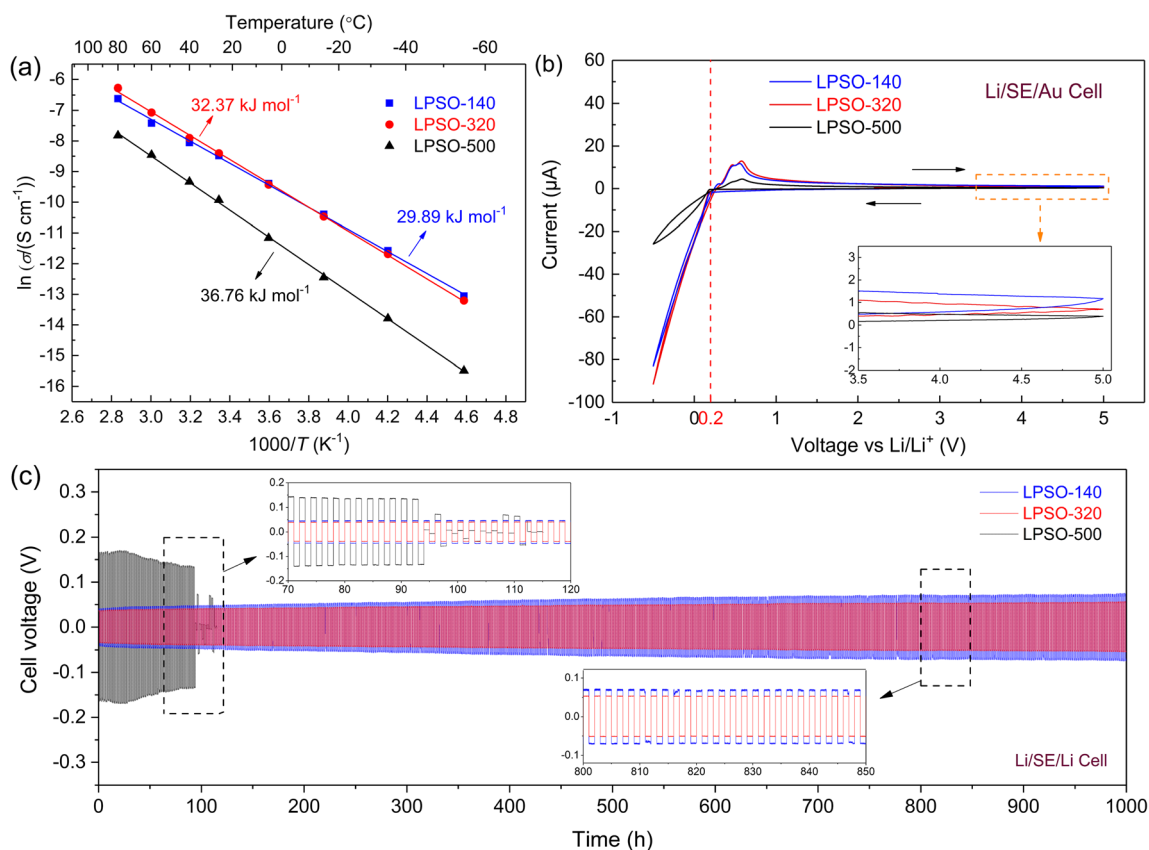


Fig. 8 **a** Arrhenius plots for the representative LPSO-140, LPSO-320, and LPSO-500 samples tested from -55 to 80 °C. **b** CV curves of Li/SE/Au cells at a scan rate of 1 mV s^{-1} between -0.5 and 5 V (vs. Li/Li⁺). The insert is a partial enlarged image of the CV curves in the high potential

range, showing that no obvious side reactions occur. **c** Voltage-time profiles of the symmetric Li/SE/Li cells at a current density of 0.1 mA cm^{-2} at room temperature and the insets present the voltage profiles during the time window of 70–120 h and 800–850 h

36.76 kJ mol⁻¹, respectively. The LPSO-140 sample has the lowest activation energy among the three samples, which is originated from its high surface energy due to a large BET surface area, resulting in a lower energy barrier for lithium-ion conduction [38, 39]. Although the activation energy of the LPSO-320 sample is slightly higher than that of the LPSO-140, it is still lower than that reported in the literature [9, 14, 40, 41]. The highest activation energy is obtained in the LPSO-500 sample because of the generation of impurity phases Li₄P₂S₆ and Li₂S. It is believed that the impurity phases in solid electrolytes would lead to the high activation energy [13, 26]. Moreover, the Li₄P₂S₆ glass-ceramic electrolyte exhibited a high activation barrier of 46.26 kJ mol⁻¹ according to the report of Dietrich et al. [31].

In order to test the electrochemical stability of the representative LPSO-140, LPSO-320, and LPSO-500 solid electrolytes, the Li/SE/Au cells were assembled, in which Li and Au serve as the reference/counter and working electrodes, respectively. Figure 8b displays CV curves of the Li/SE/Au cells in a potential range from -0.5 to 5 V versus Li/Li⁺ at a scan rate of 1 mV s⁻¹. As shown, the cathodic currents corresponding to lithium deposition start at potentials just below 0.2 V as indicated by the red dotted line because of the formation of Li-Au alloys at the Au working electrode [42]. The anodic currents ascribed to lithium dissolution are derived from the de-alloying reactions of Li-Au alloys, and the three clear current peaks in the range from 0.2 to 0.6 V correspond to the following three-phase transitions: Li₃Au to Li₅Au₃, Li₅Au₃ to Li₃Au₂, and Li₃Au₂ to Li₃Au₅ [43]. Except for the lithium deposition and dissolution, no other significant reactions are observed in the scanning voltage range. This means the electrochemical window of the obtained sulfide solid electrolyte is up to 5 V. In addition, in the CV curves, the peak strength of the three samples is consistent with their ionic conductivities.

Furthermore, we assembled the symmetric Li/LPSO-140/Li, Li/LPSO-320/Li, and Li/LPSO-500/Li cells to evaluate the cyclability and long-term compatibility of electrolytes with metallic lithium. Figure 8c shows the voltage profiles of the symmetric cells cycled at 0.1 mA cm⁻². The Li/LPSO-500/Li cell with the largest impedance exhibits the highest initial voltage of 160 mV and a gradual voltage decay after 30 h, and then the voltage suddenly drops at 95 h, which is considered to be a dendrite-induced short circuit. The internal short circuit would be attributed to the existence of Li₄P₂S₆ in the LPSO-500 electrolyte. The experiments by Hood et al. [44] showed that the buffer layer at Li₄P₂S₆/Li interface is very fragile, which is easier to be destroyed than the Li₃PS₄/Li system.

In contrast, both Li/LPSO-140/Li and Li/LPSO-320/Li cells present relatively stable voltage profiles and longer life over 1000 h, demonstrating that the LPSO-140 and LPSO-320 electrolyte have excellent stability with metallic lithium.

Specifically, due to the difference of ionic conductivity, the polarization voltage of the cell Li/LPSO-140/Li is slightly higher than that of Li/LPSO-320/Li at a current density of 0.1 mA cm⁻². According to the equations:

$$\sigma = d \times I / (S \times U) \quad (2)$$

where σ is the conductivity, d is the thickness of electrolyte pellet, I is the current, S is the area of electrolyte pellet, and U is the voltage, the direct-current conductivity of the symmetric cells Li/LPSO-140/Li and Li/LPSO-320/Li at room temperature is 1.97×10^{-4} S cm⁻¹ and 2.22×10^{-4} S cm⁻¹, which are closed to that of the electrolyte evaluated by AC impedance (Fig. 6). In addition, it is noticed that the increasing rate of polarization voltage in the Li/LPSO-320/Li cell is slower than that in the Li/LPSO-140/Li cell. This could be ascribed to high crystallinity and stable crystal structure of the electrolyte, facilitating the formation of a more stable buffer layer at β -Li₃PS₄/Li interface, which can protect the electrolyte surface from deterioration.

Conclusions

75Li₂S·(25-x)P₂S₅·xP₂O₅ (mol%) solid electrolytes were successfully prepared by wet chemistry method. The XRD results show that the crystalline phase β -Li₃PS₄ is obtained for all compositions ($x = 0, 1, 2, 3, 5$ mol%) and their average crystallite size is also calculated according to the Scherrer formula. The room-temperature lithium-ion conductivity of 75Li₂S·25P₂S₅ could be enhanced by the incorporation of P₂O₅, and the electrolyte substituted with 2 mol% P₂O₅ exhibited the highest ionic conductivity of 2.53×10^{-4} S cm⁻¹ at room temperature. Subsequently, influences of heat treatment on the structure and electrochemical properties of 75Li₂S·23P₂S₅·2P₂O₅ electrolyte were systematically investigated. When the heat treatment temperature is between 140 and 320 °C, only β -Li₃PS₄ phase is detected in the sample. The LPSO-140 shows a lower activation energy of 29.89 kJ mol⁻¹, which could be attributed to its high surface energy due to a large BET surface area. The LPSO-320 exhibited the highest ionic conductivity of 2.72×10^{-4} S cm⁻¹, the lowest electronic conductivity of 4.8×10^{-9} S cm⁻¹ at room temperature, and excellent cyclability with the metallic lithium. As the temperature exceeds 320 °C, the electrolyte partially decomposes into low lithium-ion-conducting phases Li₄P₂S₆ and Li₂S, resulting in a rapid decrease in ionic conductivity. This study shows that the heat treatment process is an effective method on the improvement of stability and ionic conductivity of the sulfide-based solid electrolytes.

Authors' contributions All authors contributed to the study conception and design. Material preparation, data collection, and analysis were performed by Jiuyong Li, Weiming Liu, Xiaofeng Zhang, and Yibo Ma. The

first draft of the manuscript was written by Jiuyong Li and all authors commented on previous versions of the manuscript. All authors read and approved the final manuscript.

Funding The work was supported by funding from Youth Program of National Natural Science Foundation of China (Grant No. 21603204).

Data availability Available upon request.

Compliance with ethical standards

Conflict of interest The authors declare that they have no conflicts of interest.

Code availability Not applicable.

References

- Goodenough JB, Kim Y (2010) Challenges for rechargeable Li batteries. *Chem Mater* 22(3):587–603
- Scrosati B, Garche J (2010) Lithium batteries: status, prospects and future. *J Power Sources* 195(9):2419–2430
- Cheng F, Liang J, Tao Z, Chen J (2011) Functional materials for rechargeable batteries. *Adv Mater* 23(15):1695–1715
- Sakuda A, Hayashi A, Tatsumisago M (2013) Sulfide solid electrolyte with favorable mechanical property for all-solid-state lithium battery. *Sci Rep* 3(1):2261
- Cao C, Li ZB, Wang XL, Zhao XB, Han WQ (2014) Recent advances in inorganic solid electrolytes for lithium batteries. *Front Energy Res* 2:1–10
- Jung YS, Oh DY, Nam YJ, Park KH (2015) Issues and challenges for bulk-type all-solid-state rechargeable lithium batteries using sulfide solid electrolytes. *Isr J Chem* 55(5):472–485
- Dietrich C, Weber DA, Sedlmaier SJ, Indris S, Culver SP, Walter D, Janek J, Zeier WG (2017) Lithium ion conductivity in $\text{Li}_2\text{S-P}_2\text{S}_5$ glasses-building units and local structure evolution during the crystallization of superionic conductors Li_3PS_4 , $\text{Li}_7\text{P}_3\text{S}_{11}$ and $\text{Li}_4\text{P}_2\text{S}_7$. *J Mater Chem A* 5(34):18111–18119
- Lin Z, Liu Z, Fu W, Dudney NJ, Liang C (2013) Lithium polysulfidophosphates: a family of lithium-conducting sulfur-rich compounds for lithium-sulfur batteries. *Angew Chem Int Ed* 52(29):7460–7463
- Liu Z, Fu W, Payzant EA, Yu X, Wu Z, Dudney NJ, Kiggans J, Hong K, Rondinone AJ, Liang C (2013) Anomalous high ionic conductivity of nanoporous $\beta\text{-Li}_3\text{PS}_4$. *J Am Chem Soc* 135(3):975–978
- Muramatsu H, Hayashi A, Ohtomo T, Hama S, Tatsumisago M (2011) Structural change of $\text{Li}_2\text{S-P}_2\text{S}_5$ sulfide solid electrolytes in the atmosphere. *Solid State Ionics* 182(1):116–119
- Homma K, Yonemura M, Kobayashi T, Nagao M, Hirayama M, Kanno R (2011) Crystal structure and phase transitions of the lithium ionic conductor Li_3PS_4 . *Solid State Ionics* 182(1):53–58
- Miura A, Rosero-Navarro NC, Sakuda A, Tadanaga K, Phuc NHH, Matsuda A, Machida N, Hayashi A, Tatsumisago M (2019) Liquid-phase syntheses of sulfide electrolytes for all-solid-state lithium battery. *Nat Rev Chem* 3(3):189–198
- Xu RC, Xia XH, Yao ZJ, Wang XL, Gu CD, Tu JP (2016) Preparation of $\text{Li}_7\text{P}_3\text{S}_{11}$ glass-ceramic electrolyte by dissolution-evaporation method for all-solid-state lithium ion batteries. *Electrochim Acta* 219:235–240
- Wang H, Hood ZD, Xia Y, Liang C (2016) Fabrication of ultrathin solid electrolyte membranes of $\beta\text{-Li}_3\text{PS}_4$ nanoflakes by evaporation-induced self-assembly for all-solid-state batteries. *J Mater Chem A* 4(21):8091–8096
- Ito S, Nakakita M, Aihara Y, Uehara T, Machida N (2014) A synthesis of crystalline $\text{Li}_7\text{P}_3\text{S}_{11}$ solid electrolyte from 1,2-dimethoxyethane solvent. *J Power Sources* 271:342–345
- Phuc NHH, Totani M, Morikawa K, Muto H, Matsuda A (2016) Preparation of Li_3PS_4 solid electrolyte using ethyl acetate as synthetic medium. *Solid State Ionics* 288:240–243
- Yamamoto T, Phuc NHH, Muto H, Matsuda A (2019) Preparation of $\text{Li}_7\text{P}_2\text{S}_8\text{I}$ solid electrolyte and its application in all-solid-state lithium-ion batteries with graphite anode. *Electron Mater Lett* 15(4):409–414
- Yubuchi S, Tsukasaki H, Sakuda A, Mori S, Hayashi A, Tatsumisago M (2019) Quantitative analysis of crystallinity in an argyrodite sulfide-based solid electrolyte synthesized via solution processing. *RSC Adv* 9(25):14465–14471
- Gobet M, Greenbaum S, Sahu G, Liang C (2014) Structural evolution and Li dynamics in nanophase Li_3PS_4 by solid-state and pulsed-field gradient NMR. *Chem Mater* 26(11):3558–3564
- Tao Y, Chen S, Liu D, Peng G, Yao X, Xu X (2015) Lithium superionic conducting oxysulfide solid electrolyte with excellent stability against lithium metal for all-solid-state cells. *J Electrochem Soc* 163(2):A96–A101
- Tachez M, Malugani J-P, Mercier R, Robert G (1984) Ionic conductivity of and phase transition in lithium thiophosphate Li_3PS_4 . *Solid State Ionics* 14(3):181–185
- Brockner UPW, Cyvin BNCSJ (1986) Darstellung, Schwingungsspektrum und Normalkoordinatenanalyse des Gold-ortho-Thiophosphates, AuPS_4 . *J Raman Spectrosc* 17:257–261
- Sourisseau C, Cavagnat R, Fouassier M, Brec R, Elder SH (1995) Infrared, Raman, resonance Raman spectra and lattice dynamics calculations of the solid potassium(I) nickel(II) thiophosphate compound, KNiPS_4 . *Chem Phys* 195(1-3):351–369
- Sang L, Haasch RT, Gewirth AA, Nuzzo RG (2017) Evolution at the solid electrolyte/gold electrode interface during lithium deposition and stripping. *Chem Mater* 29(7):3029–3037
- Xie D, Chen S, Zhang Z, Ren J, Yao L, Wu L, Yao X, Xu X (2018) High ion conductive Sb_2O_5 -doped $\beta\text{-Li}_3\text{PS}_4$ with excellent stability against Li for all-solid-state lithium batteries. *J Power Sources* 389:140–147
- Mizuno F, Hayashi A, Tadanaga K, Tatsumisago M (2006) High lithium ion conducting glass-ceramics in the system $\text{Li}_2\text{S-P}_2\text{S}_5$. *Solid State Ionics* 177(26–32):2721–2725
- Wang X, Xiao R, Li H, Chen L (2016) Oxygen-driven transition from two-dimensional to three-dimensional transport behaviour in $\beta\text{-Li}_3\text{PS}_4$ electrolyte. *Phys Chem Chem Phys* 18(31):21269–21277
- Hayashi A, Muramatsu H, Ohtomo T, Hama S, Tatsumisago M (2014) Improved chemical stability and cyclability in $\text{Li}_2\text{S-P}_2\text{S}_5\text{-P}_2\text{O}_5\text{-ZnO}$ composite electrolytes for all-solid-state rechargeable lithium batteries. *J Alloys Compd* 591:247–250
- Xiao R, Li H, Chen L (2015) High-throughput design and optimization of fast lithium ion conductors by the combination of bond-valence method and density functional theory. *Sci Rep* 5(1):14227
- de Klerk NJJ, van der Maas E, Wagemaker M (2018) Analysis of diffusion in solid-state electrolytes through MD simulations, improvement of the Li-ion conductivity in $\beta\text{-Li}_3\text{PS}_4$ as an example. *ACS Appl Energy Mater* 1(7):3230–3242
- Dietrich C, Sadowski M, Siculo S, Weber DA, Sedlmaier SJ, Weldert KS, Indris S, Albe K, Janek J, Zeier WG (2016) Local structural investigations, defect formation, and ionic conductivity of the lithium ionic conductor $\text{Li}_4\text{P}_2\text{S}_6$. *Chem Mater* 28(23):8764–8773
- Han F, Yue J, Fan X, Gao T, Luo C, Ma Z, Suo L, Wang C (2016) High-performance all-solid-state lithium-sulfur battery enabled by a mixed-conductive Li_2S nanocomposite. *Nano Lett* 16(7):4521–4527

33. Chen Y, Cai L, Liu Z, dela Cruz CR, Liang C, An K (2015) Correlation of anisotropy and directional conduction in β -Li₃PS₄ fast Li⁺ conductor. *Appl Phys Lett* 107(1):013904
34. C. Yu J, Xu A, Zhang L, Song R, Wu L (2004) Synthesis and characterization of porous magnesium hydroxide and oxide nanoplates. *J Phys Chem B* 108(1):64–70
35. Kamaya N, Homma K, Yamakawa Y, Hirayama M, Kanno R, Yonemura M, Ta K, Kato Y, Hama S, Kawamoto K, Mitsui A (2011) A lithium superionic conductor. *Nat Mater* 10(9):682–686
36. Han F, Westover AS, Yue J, Fan X, Wang F, Chi M, Leonard DN, Dudney NJ, Wang H, Wang C (2019) High electronic conductivity as the origin of lithium dendrite formation within solid electrolytes. *Nat Energy* 4(3):187–196
37. Yu K, Gu R, Wu L, Sun H, Ma R, Jin L, Xu Y, Xu Z, Wei X (2018) Ionic and electronic conductivity of solid electrolyte Li_{0.5}La_{0.5}TiO₃ doped with LiO₂-SiO₂-B₂O₃ glass. *J Alloys Compd* 739:892–896
38. Maier J (2004) Ionic transport in nano-sized systems. *Solid State Ionics* 175(1–4):7–12
39. Puina W, Rodewald S, Ramlaub R, Heitjans P, Maier J (2000) Local and overall ionic conductivity in nanocrystalline CaF₂. *Solid State Ionics* 131(1):159–164
40. Teragawa S, Aso K, Tadanaga K, Hayashi A, Tatsumisago M (2014) Liquid-phase synthesis of a Li₃PS₄ solid electrolyte using N-methylformamide for all-solid-state lithium batteries. *J Mater Chem A* 2(14):5095–5099
41. Phuc NHH, Morikawa K, Mitsuhiro T, Muto H, Matsuda A (2017) Synthesis of plate-like Li₃PS₄ solid electrolyte via liquid-phase shaking for all-solid-state lithium batteries. *Ionics* 23(8):2061–2067
42. Bach P, Stratmann M, Valencia-Jaime I, Romero AH, Renner FU (2015) Lithiation and delithiation mechanisms of gold thin film model anodes for lithium ion batteries: electrochemical characterization. *Electrochim Acta* 164:81–89
43. Bach P, Valencia-Jaime I, Rütt U, Gutowski O, Romero AH, Renner FU (2016) Electrochemical lithiation cycles of gold anodes observed by in situ high-energy X-ray diffraction. *Chem Mater* 28(9):2941–2948
44. Hood ZD, Kates C, Kirkham M, Adhikari S, Liang C, Holzwarth NAW (2016) Structural and electrolyte properties of Li₄P₂S₆. *Solid State Ionics* 284:61–70

Publisher's note Springer Nature remains neutral with regard to jurisdictional claims in published maps and institutional affiliations.